

Early results from GLASS-JWST XIV: A first morphological atlas of the $1 < z < 5$ Universe in the rest-frame optical

C. JACOBS,^{1,2} K. GLAZEBROOK,¹ A. CALABRÒ,³ T. TREU,⁴ T. NANNAYAKKARA,^{1,2} T. JONES,⁵ E. MERLIN,³
R. ABRAHAM,^{6,7} A. R. H. STEVENS,^{8,2} B. VULCANI,⁹ L. YANG,¹⁰ A. BONCHI,^{3,11} K. BOYETT,^{12,2} M. BRADAC,^{13,5}
M. CASTELLANO,¹⁴ A. FONTANA,¹⁴ D. MARCHESINI,¹⁵ M. MALKAN,⁴ C. MASON,^{16,17} T. MORISHITA,¹⁸ D. PARIS,³
P. SANTINI,³ M. TRENTI,^{12,2} AND X. WANG¹⁸

¹Centre for Astrophysics and Supercomputing, Swinburne University of Technology, PO Box 218, Hawthorn, VIC 3122, Australia

²ARC Centre of Excellence for All Sky Astrophysics in 3 Dimensions (ASTRO 3D), Australia

³INAF Osservatorio Astronomico di Roma, Via Frascati 33, 00078 Monteporzio Catone, Rome, Italy

⁴Department of Physics and Astronomy, University of California, Los Angeles, 430 Portola Plaza, Los Angeles, CA 90095, US

⁵Department of Physics and Astronomy, University of California Davis, 1 Shields Avenue, Davis, CA 95616, USA

⁶Department of Astronomy & Astrophysics, University of Toronto, Toronto, ON M5S 3H4, Canada

⁷Dunlap Institute for Astronomy and Astrophysics, University of Toronto, Toronto ON, M5S 3H4, Canada

⁸International Centre for Radio Astronomy Research, The University of Western Australia, Crawley, WA 6009, Australia

⁹INAF Osservatorio Astronomico di Padova, vicolo dell'Osservatorio 5, 35122 Padova, Italy

¹⁰Kavli Institute for the Physics and Mathematics of the Universe, The University of Tokyo, Kashiwa, Japan 277-8583

¹¹ASI-Space Science Data Center, Via del Politecnico, I-00133 Roma, Italy

¹²School of Physics, University of Melbourne, Parkville 3010, VIC, Australia

¹³University of Ljubljana, Department of Mathematics and Physics, Jadranska ulica 19, SI-1000 Ljubljana, Slovenia

¹⁴INAF - Osservatorio Astronomico di Roma, via di Frascati 33, 00078 Monte Porzio Catone, Italy

¹⁵Department of Physics and Astronomy, Tufts University, 574 Boston Ave., Medford, MA 02155, USA

¹⁶Cosmic Dawn Center (DAWN)

¹⁷Niels Bohr Institute, University of Copenhagen, Jagtvej 128, 2200 København N, Denmark

¹⁸IPAC, California Institute of Technology, MC 314-6, 1200 E. California Boulevard, Pasadena, CA 91125, USA

(Received; Revised April 18, 2023; Accepted April 18, 2023)

Submitted to ApJ

ABSTRACT

We present a rest-frame optical morphological analysis of galaxies observed with the NIRC*am* imager on the James Webb Space Telescope (JWST) as part of the GLASS-JWST Early Release Science program. We select 388 sources at redshifts $0.8 < z < 5.4$ and use the seven $0.9\text{--}5\mu\text{m}$ NIRC*am* filters to generate rest-frame *gri* composite color images, and conduct visual morphological classification. Compared to HST-based work we find a higher incidence of disks and bulges than expected at $z > 1.5$, revealed by rest frame optical imaging. We detect 123 clear disks (58 at $z > 1.5$) of which 76 have bulges. No evolution of bulge fraction with redshift is evident: 61% at $z < 2$ ($N = 110$) versus 60% at $z \geq 2$ ($N = 13$). A stellar mass dependence is evident, with bulges visible in 80% of all disk galaxies with mass $> 10^{9.5} M_{\odot}$ ($N = 41$) but only 52% at $M < 10^{9.5} M_{\odot}$ ($N = 82$). We supplement visual morphologies with non-parametric measurements of Gini and Asymmetry coefficients in the rest-frame *i*-band. Our sources are more asymmetric than local galaxies, with slightly higher Gini values. When compared to high-*z* rest-frame ultraviolet measurements with Hubble Space Telescope, JWST shows more regular morphological types such as disks, bulges and spiral arms at $z > 1.5$, with smoother (i.e. lower Gini) and more symmetrical light distributions.

Keywords: catalogs: surveys

1. INTRODUCTION

Many questions remain regarding the evolution of galaxies in the Universe's early epochs. Two key observables, namely morphology and rest-frame optical col-

ors, are closely tied to many important galaxy properties such as stellar mass distribution and dynamical scale. Morphological studies have played a key role since the earliest days of extragalactic astronomy; Hubble's

(1926) ‘tuning fork’ morphological classification system is still in widespread use, and research continues into when in the Universe’s history the earliest irregular, clumpy progenitors give way to the regular morphological types it depicts (see [Conselice 2014](#) for a review). Previous work, driven primarily by deep Hubble Space Telescope (HST) observations, determined that the modern Hubble sequence was not yet in place by $z \sim 1.5$ ([Elmegreen et al. 2007](#); [Abraham et al. 2007](#); [Conselice et al. 2011](#); [Elmegreen & Elmegreen 2013](#); [Abraham et al. 1996a](#)). At $z > 2$ the galaxy population is dominated by irregular morphologies ([Conselice et al. 2005](#); [van Dokkum et al. 2013](#); [Buitrago et al. 2013](#); [Conselice 2014](#)), while kinematic observations suggest an epoch of early disk assembly (e.g. [Simons et al. 2017](#); [Wisnioski et al. 2015](#); see [Glazebrook 2013](#) for a review). A key challenge for high-redshift morphology studies is that rest-frame optical imaging is required to probe the bulk of the stellar population. HST can obtain rest-frame optical images at $z \lesssim 2.5$ (reaching wavelengths $\lambda \leq 1.7 \mu\text{m}$). At higher redshifts HST probes only the rest-frame UV, which is dominated by patchy emission from young and unobscured star-forming regions. Furthermore, accurate rest-frame optical colors spanning the 4000 Å break, a classical signature of age and stellar mass, are limited to $z < 1.5$. While the Spitzer Space Telescope provided imaging at longer wavelengths, it could not spatially resolve high-redshift galaxies. The commissioning of the James Webb Space Telescope (JWST; [Gardner 2006](#)), with its diffraction-limited infrared imaging capabilities, now offers us a first clear view of rest-frame optical galaxy morphology in the high-redshift universe. This new era in infrared astronomy will reveal previously hidden details about galaxies in the first billion years of cosmic history.

Morphological features — such as the presence or absence of a disk or bulge — are correlated with a galaxy’s stellar and halo masses (e.g., [Calvi et al. 2012](#); [Correa & Schaye 2020](#)); environment (e.g., [Dressler 1984](#); [Blanton & Moustakas 2009](#)); evolutionary history such as the role of mergers versus in-situ star formation ([Conselice 2008](#)); feedback and gas accretion from the cosmic web; the build-up of angular momentum ([Fall 1983](#); [Sweet et al. 2020](#)); and star formation rate (e.g., [Dimauro et al. 2022](#)). Morphological studies will play a key role in understanding the redshift evolution of these properties and in building up a complete picture of how the modern Universe came to be. Just as in Hubble’s day, many morphological studies still rely on visual classification by experts (e.g., [Driver et al. 2022](#)). This is supplemented by newer methods such as citizen science (e.g., [Lintott et al. 2011](#)) and the use of machine learning (e.g., [Dieleman](#)

[et al. 2015](#); [Zhu et al. 2019](#)). Non-parametric methods such as Concentration-Asymmetry (CA, [Abraham et al. 1994](#)) and Concentration-Asymmetry-Smoothing (CAS, [Conselice et al. 2000](#)), which are based solely on photometric measurements, enable a more objective comparison between galaxy populations. Here we employ both subjective and non-parametric methods, including the Gini coefficient ([Abraham et al. 2003](#); [Conselice 2014](#)), in order to make a first characterization of the population of galaxies at $z \gtrsim 1$ revealed by JWST imaging. We choose a non-parametric approach rather than model-fitting with e.g. GALFIT ([Peng et al. 2010](#)), as the former assumes no underlying luminosity profile and does not require a detailed Point Spread Function (PSF) model. Non-parametric methods are also more readily applied to the asymmetric irregular galaxies which are expected to be prevalent at high redshifts.

In this paper, we examine the rest-frame optical morphologies of galaxies and their trends with redshift reaching up to $z \gtrsim 5$. This paper is among the first investigations of galaxies in this newly accessible parameter space of color and redshift. Our study is based on GLASS-JWST, which provides the deepest photometry of the 13 JWST Early Release Science Programs. It is obtaining NIRISS ([Doyon et al. 2012](#); [Willott et al. 2022](#)) and NIRSpect ([Jakobsen et al. 2022](#)) spectroscopy in the center of the galaxy cluster Abell 2744, while obtaining NIRCcam images of two parallel fields. Details can be found in the survey paper ([Treu et al. 2022](#)). Here we present initial results from morphological inspection of 388 sources out to redshift 5.5 from a GLASS-JWST NIRCcam parallel field. We produce postage stamp images in rest-frame *gri* colors, manually classify their morphology, and calculate non-parametric asymmetry and Gini coefficient values to enable comparisons with other galaxy populations. While this is merely a snapshot of the high-redshift infrared data to come, this analysis already allows us to place new constraints on morphological fractions out to $z \sim 5$.

Whereas this paper focuses on the appearance of galaxies after reionization is complete, we note that the morphology of galaxies in the epoch of reionization at $z > 7$ is discussed in a companion paper ([Treu et al. 2022](#), Paper XII).

This paper is structured as follows. In Section 2, we discuss the imaging data and the process of selecting our morphological sample. In Section 3, we describe the results of our visual classification and compare measurements to the $z \sim 0$ galaxy population and to previous high- z rest-frame UV analyses. We offer concluding remarks in Section 4. We adopt a standard cosmology with $\Omega_m = 0.3$, $\Omega_\Lambda = 0.7$, and $H_0 = 70 \text{ km s}^{-1} \text{ Mpc}^{-1}$.

All magnitudes are in the AB system (Oke & Gunn 1983).

2. METHODOLOGY

2.1. Data

On June 28–29 and November 10–11th 2022, the GLASS-JWST Early Release Science (ERS) program used the NIRISS wide-field slitless spectrograph and NIRC*am* imager to observe the Abell 2744 lensing cluster. While the cluster core was observed with the grism spectrograph, NIRC*am* imaging was taken in parallel mode in seven bands from $\sim 1\text{--}5\ \mu\text{m}$: F090W, F115W, F150W, F200W, F277W, F356W and F444W. The data were reduced using the NIRC*am* calibration files (cjwst 1014.pmap to cjwst 1019.pmap) provided by STScI. The F444W band was selected for source detection and all images were point-spread function (PSF) matched to this band producing a catalog reaching typical $5\text{-}\sigma$ depths of ~ 30.2 mag in all bands. More details regarding the observations, data reduction, and catalog generation can be found in (Paris et al. 2023, Paper II) and (Merlin et al. 2022, Paper II). Although the parallel fields are in the vicinity of the cluster Abell 2744, they are sufficiently offset from the cluster core that we expect lensing magnification to be a modest effect (Medezinski et al. 2016) which does not affect morphological classification. The Gini coefficient is also robust to lensing effects.

2.2. Catalog and target selection

We start with the GLASS-JWST source catalog (Paper II), which is the result of running Source Extractor (Bertin & Arnouts 1996) on the F444W imaging and selecting sources with signal-to-noise ratio greater than 2. This yields a catalog of 6689 sources. In order to improve the quality of photometric redshifts, for the other six bands, we match the PSFs to the F444W band and perform aperture photometry in 6 circular apertures between 0.2 and 2.2 arcsec in diameter. This is solely for the purposes of photometry; we perform a different PSF matching to construct our color images described in Section 2.3 below. The final catalog has a 5σ magnitude limit of 29.7 in F444W.

Since we will compare our NIRC*am* sample with the lower-redshift Universe, we select sources where morphology will be detectable and approximate rest-frame optical colors can be seen. Firstly, as per Nanayakkara et al. (2022, Paper XVI), we obtain photometric redshifts with the EAZY (Brammer et al. 2008) photomet-

ric redshift code using `easy_v1.3.spectra.param` templates provided by the software and total flux measured in a 0.45 arcsec aperture (i.e., $3\times\text{FWHM}$; Paper II). We select all galaxies that have $S/N > 5$ detections in all GLASS-JWST bands and visually inspect the quality of the SED fits. To produce RGB images that are both close to visual true color and adopt a common convention for RGB visualization of local sources, we choose rest-frame *irg* bands as our RGB channels respectively. In order to produce images corresponding to these bands in the local Universe, we select targets in five redshift ranges such that there is an overlap greater than 50% in three of our observed filters with rest-frame *gri* (from SDSS; York et al. 2000) bands. These redshift ranges span $0.8 < z < 5.4$ and are summarized in Table 1.

After filtering our catalog to photometric redshifts in these ranges, we assemble a total of 1318 sources for further study. Next, we discard sources that have masked-out pixels inside a 100×100 pixel postage stamp, and sources with noise in any of the *gri*-analog filters which is ≥ 3 times the mean for that band. The latter filters out sources at the edge of the detector. We inspected a subset of the remaining images, and found that the following criteria produced a sample of galaxies with sufficient size and brightness to have discernible morphology. We first discard sources where the F444W segmentation map contains fewer than 400 pixels. Then, we limit our sample to sources brighter than $\text{mag} < 27$ in F444W and < 26 in the analog *i*-band. Applying these cuts results in a sample of 434 sources. The median effective radius of discarded sources is 5.7 pixels (.18 arcsec). The median integrated S/N in the bands used for morphological classification was ~ 60 . Although only a small portion of the full GLASS catalog, this sample size is large enough to provide the first characterization of the morphologies of the $1 < z < 5$ galaxy population. Finally, we obtain stellar mass estimates using the FAST++ code (Schreiber et al. 2018) as outlined in Paper XVI. We use Bruzual & Charlot (2003) stellar population models with a Chabrier (2003) IMF, a truncated SFH with a constant and an exponentially declining SFH component, and a Calzetti et al. (2000) dust law. Associated errors on stellar masses obtained using SED fitting are estimated to be ~ 0.3 dex (Conroy 2013), which can be higher for fainter $m_{\text{F150W}} > 28$ sources at $z > 2$. Using these masses we determine the 80% stellar mass completeness threshold, listed in Table 1: for the range $4.4 < z < 5.4$ the sample is 50% complete above $M_* = 9.52$.

Table 1. The redshift ranges for which $> 50\%$ overlap exists between rest-frame SDSS *gri* filters and JWST NIRC*am* filters, enabling us to inspect the morphology of high-redshift galaxies consistently in rest-frame optical colors. The number of sources in our final sample in each redshift range is also indicated, along with the morphological fractions as percentages for peculiar/elliptical/disk. We also show the stellar mass 80% completeness threshold, in units of $\log M_*/M_\odot$, estimated by comparing to the original catalog in the same redshift range.

Redshift range	Bands used (RGB)	80% comp. ($\log M_*/M_\odot$)	# sources	Morph. frac. (pec/ell/disk)
0.8–1.1	F090W, F115W, F150W	9.4	116	37/18/46%
1.4–1.7	F115W, F150W, F200W	10.1	223	52/17/32%
2.4–2.6	F150W, F200W, F277W	9.4	22	45/20/35%
3.4–3.7	F200W, F277W, F356W	9.0	34	62/28/9%
4.4–5.4	F277W, F356W, F444W	9.5*	39	61/30/9%
Total			434	

* In this bin we use 50% completeness due to low number statistics.

We also assemble two reference samples. Firstly, a catalog of 1000 local galaxies from SDSS DR17 (Blanton et al. 2017), randomly selected from those with spectroscopic redshifts $0.01 < z < 0.03$, *i*-band magnitude < 22 , and stellar masses between 10^8 and $10^{11} M_\odot$, which we use as a local baseline for the non-parametric morphological analysis. Secondly, a catalog of 369 sources within our redshift ranges taken from the ZFOURGE (Straatman et al. 2016) survey that lie in the Chandra Deep Field-South (CDFS; Xue et al. 2011), along with corresponding F814W HST imaging. We use these galaxies to compare our sample to high-redshift rest-frame UV observations.

2.3. Making rest-frame *gri* color images

In order to produce color images we must first match the angular resolution of different NIRC*am* filters. We obtain PSFs using the WebbPSF package provided by STScI. We then calculate a matched kernel for each combination of bands in Table 1, using the PHOTUTILS (Bradley et al. 2020) PYTHON package, such that the bluest and middle bands are PSF-matched to the reddest band. We find that for the 3 filters blueward of F200W, creating a matching kernel of sufficient quality to produce few visible artifacts was difficult, so in creating RGB images we have used non-PSF-matched imaging for these filters. Redward of F200W we have used PSF-matched imaging.

We construct RGB images using the filters in Table 1 according to the Lupton et al. (2004) and Trilogy (Coe et al. 2012) algorithms. To create the images in Figure 1, we used the Lupton HumVI code (Marshall et al. 2015) with the parameters $Q = 1.1$, $\alpha = 412$, and the *gri* bands

weighted as follows: (0.9, 1.0, 1.3). For visual inspection (see Section 2.4) we examine RGB images using four different sets of scaling parameters, with differing levels of dynamic range: the Lupton scaling, two logarithmic scalings with different noise luminosity (Trilogy), and a linear scaling.

2.4. Morphological classification

Eight authors (CJ, KG, AC, TT, TJ, RA, MM, DM) inspected RGB images of each of the 434 selected NIRC*am* sources and classified sufficiently resolved sources (see Section 2.2) into four broad categories: peculiar (no clear regular shape), elliptical/S0 (spherical or oblate spheroid—greater than PSF), disk (face on or clear, symmetric disk extended shape), and disk+bulge (clear central concentration detectable). Where the classification was too uncertain due to magnitude or resolution, the source was flagged as such. Sources were examined as RGB images with 4 different scalings as well as monochrome images in all seven bands using the MORPHRATER¹ software package designed for this purpose. Discarding sources with more than one flag left 388 sources which forms our final sample for the analysis in this paper. In the following, each source is assigned to the category with the highest number of classifications. Across our sample, the median level of agreement was high – 5/8 of the inspectors. This good agreement is likely due to the broad categories used as well as the cuts made to ensure that sources were sufficiently resolved to make a good determination.

¹ <https://github.com/coljac/morphrater>

2.5. Non-parametric measurements

For each of our sources we automatically calculate values of the Gini coefficient (G) and asymmetry (A) parameters from the rest-frame i -band images, following the formulation of Abraham et al. (1996b) and Abraham et al. (2007). The Gini coefficient is high in concentrated and symmetrical early type galaxies, and is more robust against isophote thresholds than the standard concentration parameter (Abraham et al. 2007), but can also be high in asymmetrical late type galaxies dominated by a few bright clumps. The asymmetry parameter A is determined by calculating the residual difference of a galaxy with its own rotated image, along with a noise correction (per Abraham et al. 1996a; Lotz et al. 2004). A represents the ratio of light remaining to the original object flux, thus a perfectly symmetric source would have $A = 0$. The axis of rotation is the brightest pixel within a 40×40 pixel box around the center of each source as identified by Source Extractor. These measurements, along with (e.g.) clumpiness (Conselice 2003), multiplicity (Law et al. 2007), and others (Freeman et al. 2013, e.g.) are well established in the literature and have been used previously to probe the relationship between optical/UV morphologies in HST (Lee et al. 2013; Mager et al. 2018) and the evolution with redshift (Whitney et al. 2021, e.g.).

3. RESULTS AND DISCUSSION

3.1. Prevalence of disks, bulges and spiral structure

In Figure 1 we present a sample of sources from across the selected redshift ranges and mass bins. These sources are typical of the overall sample for those with a discernible morphology. (Several gaps in the figure were filled by extending the redshift bins by up to 0.1; these are indicated by lack of morphological designation.) As expected, at $0.8 < z < 5.4$, we find a significantly higher proportion of peculiar morphologies than in the local Universe, where peculiars make up less than 5% of galaxies (Murata et al. 2014). Peculiars make up 42% of the sample at $z < 2$, and 54% at higher redshifts. We do not see a significant increase with redshift, but this may be due to selection effects, as higher masses are over-represented in the higher redshift sample. The fraction of peculiar galaxies is 50% at stellar masses $< 10^{9.5} M_{\odot}$, and 24% at higher mass.

The presence of visible disks (both edge- and face-on) is detected in many galaxies, and we see clear spiral structure up to $z = 2.4$. Many of the disks show clear bulges, again up to $z = 2.4$. As can be seen in Figure 1, there are sources of unambiguous typical Sa/Sb morphology beyond redshift 2. Several sources additionally show distinct bars.

For reference, Figure 2 shows several examples of local disk galaxies (in gri RGB images) artificially redshifted to three of our redshift bands, as they would appear in NIRC*am* images. The effects of K-correction and bandpass shifting have not been considered for the purposes of this illustration; the former as it is a small effect for these bright sources (Barden et al. 2008), and the latter as our methodology relies on the good agreement between the bandpasses of the rest-frame SDSS bands and their high- z NIRC*am* analogs. The scale and colors of these local galaxies can be compared to sources at similar redshifts in Figure 1. While these images are larger (here 8 arcsec, c.f. 3-arcsec stamps in Figure 1), many of the sources we observe at $z > 2$ appear morphologically similar to the local SDSS galaxies although with typically higher surface brightness.

Overall, we see strong clues that the Hubble sequence is well developed by $z = 1.5$. The current generation of cosmological hydrodynamic simulations, such as TNG50 (the highest-resolution run of the IllustrisTNG suite), do predict a significant proportion of disks in star-forming galaxies at high redshifts, for instance $\sim 30\%$ at $z \simeq 3$ and $\sim 50\%$ at $z \simeq 2$ for $M \gtrsim 10^{9.5} M_{\odot}$ (Pillepich et al. 2019, see their Figure 9), and moreover predict a population of well-developed spirals with bulges at $z = 2$ visible in rest-frame optical (although this may be sensitive to decomposition morphology; see Zana et al. 2022). As additional JWST imaging data becomes available over wider fields, we will be better able to empirically confirm (or challenge) these predictions.

In some aspects, this work is in tension with HST studies. Mortlock et al. (2013) found few disks among massive ($M_{*} > 10^{10} M_{\odot}$) galaxies above $z > 2$ with peculiars dominating; we find 40% disks in this mass range at $z > 2$. Whitney et al. (2021) find more asymmetry and higher concentration for a given mass; we find a weak trend only. Huertas-Company et al. (2015), who examine morphological evolution in CANDELS galaxies, find irregulars dominant for $2 < z < 3$, with regular disks/disk and bulges dominating below $z = 2$; in our higher mass bin, we find disks dominate by $z = 3$ and peculiars are $\sim 10\%$ by $z = 2$. Tacchella et al. (2015) find preponderance of disk structures in 29 $z \sim 2$ galaxies, with 40% sporting large ($B/T > 0.3$) bulges, perhaps closer to our finding but for a much smaller sample.

Otherwise, several studies predict our finding that rest-frame UV-limited observations will lead to clumpier classifications. Lee et al. (2013) perform a non-parametric analysis that quantifies this effect. Kartaltepe et al. (2015) report that galaxies observed in the UV may appear irregular when in reality are normal disks in the optical. Mager et al. (2018) also perform

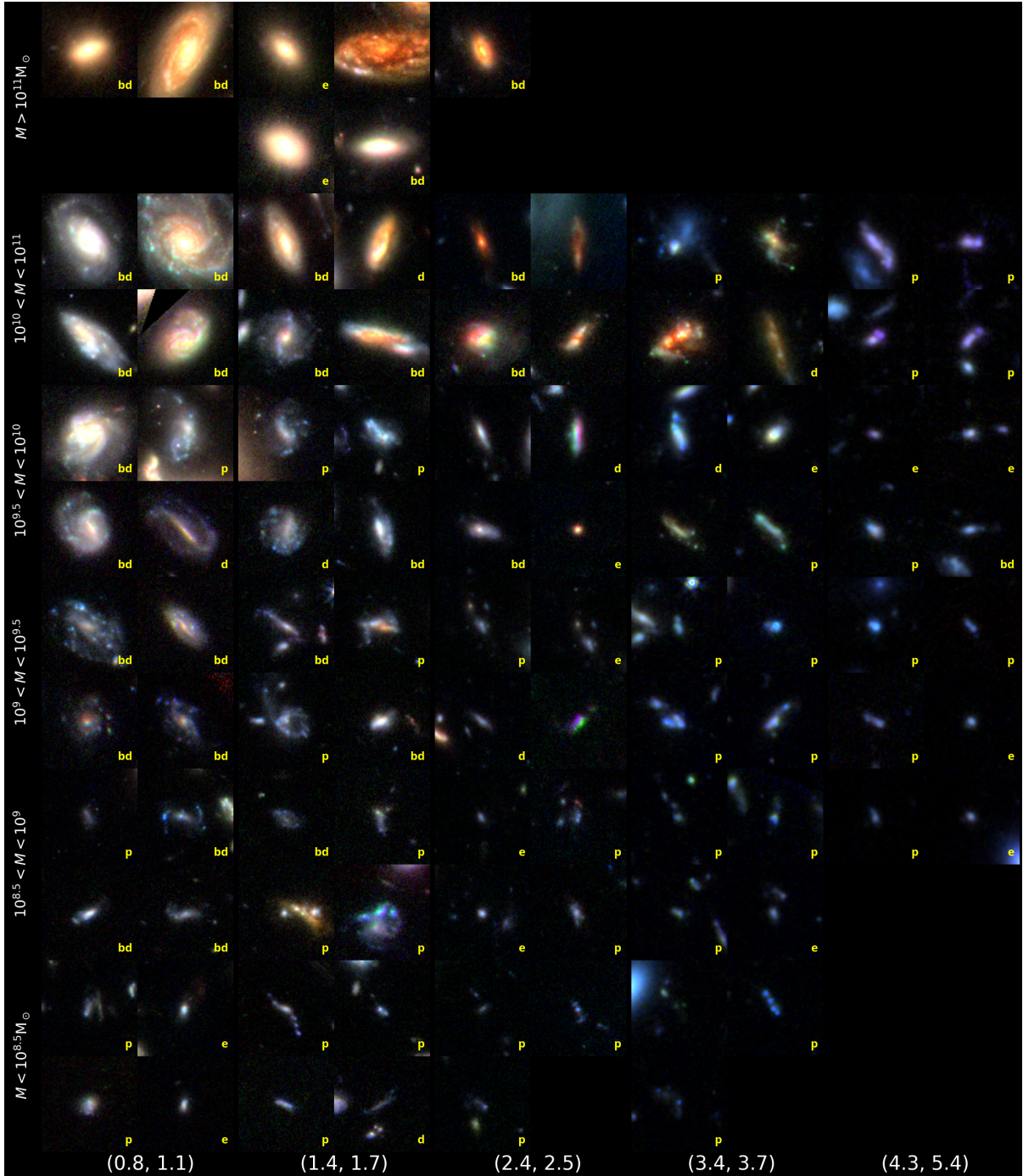


Figure 1. Rest-frame *gri* RGB images of selected sources organized by redshift bin (indicated at bottom, increasing left to right) and mass bin (indicated at left, decreasing top to bottom). Each postage stamp is 3.1 arcsec wide. Morphological classifications are indicated, where p=peculiar, e=elliptical, d=disk and bd=bulge and disk.

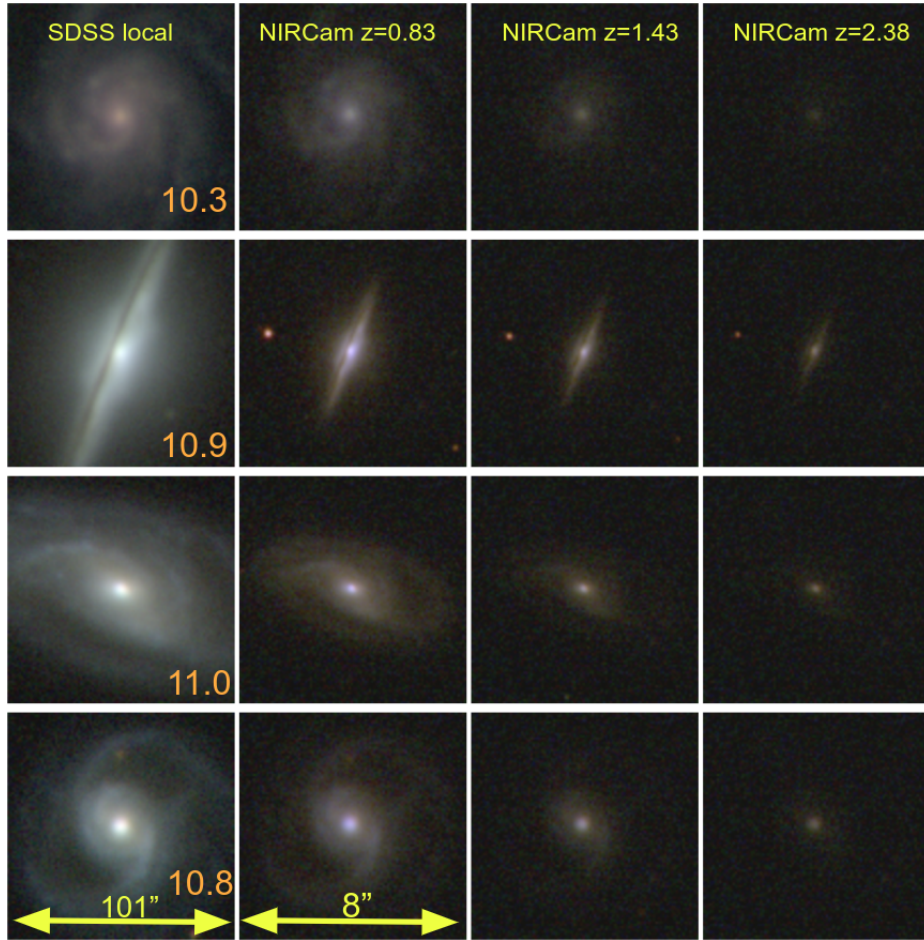


Figure 2. RGB images of SDSS galaxies in SDSS *gri* bands (left) and simulated NIRCam observations at $z = 0.83$, $z = 1.43$ and $z = 2.38$ in *gri* analogs, per Table 1. The stellar masses ($\log M_*/M_\odot$) are indicated in orange. The SDSS images are 101 arcsec on a side, while the NIRCam simulations are 8 arcsec; the physical dimensions are 54, 34, 25 and 52 kpc from top to bottom.

CAS analysis and find galaxies appearing more symmetric (early type) at longer wavelengths for GALEX (Bianchi & GALEX Team 1999) UV observations.

Although our sample includes some merging and interacting galaxies, we have not controlled for environment in this analysis. We have not considered whether a source may be interacting with neighbors, and whether this affects the morphologies due to features such as tidal tails.

3.2. Trends by mass and redshift

We now consider evolutionary trends with stellar mass and redshift revealed by our sample. Because we expect uncertainties of ~ 0.3 dex on our estimated stellar masses (Section 2.2), we bin our sources into six stellar mass ranges of 0.5 dex width as shown in Figure 1 (from $M_* < 10^{8.5} M_\odot$ to $> 10^{11} M_\odot$). We find an abundance of clumpy/peculiar galaxies across all mass bins. Bulges and disks are visible across the mass range $M_* > 10^{8.5} M_\odot$, and a significant population of spirals with bulges is apparent at $M_* > 10^{9.5} M_\odot$.

In Figure 3 we depict the broad morphological classification as a fraction of the sample by (photometric) redshift and mass bins. Here we divide the sample into two mass bins (limited by our sample size), greater or less than $10^{9.5} M_\odot$. The redshift bins correspond to the same ranges chosen for their overlap with rest-frame optical filters (Section 2.2). The blue points represent the combined contribution of “disk” and “disk+bulge” morphologies, while the “disk+bulge” fraction is also shown separately with dashed lines. We see that by $z \simeq 2.4$ there is a significant proportion of disky galaxies in our sample ($\sim 20\%$ even for the low-mass bin, and the vast majority in the high-mass end), and at higher masses the majority have a recognisable bulge. The proportion of noticeable Sc/SBCs increases below redshift 2.4 as can be seen in Figure 1. Counter-intuitively, the proportion of peculiar morphologies for low-mass galaxies shows only a weak downwards evolution with decreasing redshift; previous work has suggested that by $z \sim 1$ the irregular number and mass fraction is dropping rapidly (e.g., Oesch et al. 2010). A larger sample size at high redshift may resolve this apparent anomaly.

At all redshifts and mass ranges, our sample is significantly bluer in the optical than local galaxies. The mean $g - i$ color of the 388 sources in our morphological catalog is 0.22 (with scatter $\sigma = 0.36$), whereas the $z \sim 0$ comparison sample from SDSS has a mean $g - i = 0.80$ ($\sigma = 0.37$). Galaxies in our highest redshift bins (3.36–5.43) are bluest, with a mean rest-frame $g - i$ of -0.12 ($\sigma = 0.35$). This is consistent with the large UV slopes seen at high redshifts (e.g., see Paper XVI).

3.3. Gini and Asymmetry

The results of the Gini–Asymmetry (GA) analysis are shown in Figure 4. Here we show the sample of this paper (color-coded by visual classification), the SDSS local comparison sample (top panel, in grey), and our HST F814W sample (bottom panel, in orange). Histograms of the statistics are also shown for the three samples. The JWST GA diagram shows a remarkable agreement with the visual morphologies – disks and ellipticals have low A , ellipticals have high G , and peculiar galaxies have high A .

The comparison with SDSS shows similar distributions, with the JWST sample being skewed to both higher A (0.27 ± 0.01 vs. 0.19 ± 0.01 for SDSS) and higher G values (0.49 ± 0.01 vs. 0.45 ± 0.01 for SDSS). We interpret this difference as arising from the overall younger age of the high-redshift population, with both coefficients being driven up the prevalence of intense knots of star-formation. Naïvely, we might have expected more separation between the JWST and SDSS populations. However, as can be seen from the images in Figure 1, many galaxies in our sample have close morphological analogs in the local Universe.

Compared to the HST rest-frame UV sample, our sample is significantly more symmetrical (mean $A = 0.26 \pm 0.01$ vs HST 0.41 ± 0.01) and with lower G (mean 0.51 ± 0.01 vs HST 0.64 ± 0.01). The increased depth of the NIRCcam imaging needs to be considered, as we are probing significantly lower masses at each redshift range compared to HST. In the bottom panel of Figure 4 we show the difference when the sample is mass-matched to the HST range. In the five redshift ranges, the HST mass limits are 8.8, 9.4, 9.5, 9.9, and 10.4 $\log M/M_\odot$ respectively. The mean Gini coefficient for the NIRCcam subsample ($N=67$) is 0.57 ± 0.01 , with mean A lower at 0.22 ± 0.02 .

The HST sample shows many galaxies with high values of G and/or A . Inspection of the F814W images show these are star-forming clumpy systems and they have blue colors. The clumpiness in the rest-UV gives rise to high G values, and they are often highly asymmetrical. In contrast the NIRCcam sample is much smoother (giving rise to the lower G) and more symmetrical (lower A). We interpret this as an effect of the rest-frame optical being a much better tracer of the stellar mass, compared to the rest-UV which traces low mass-to-light ratio star-forming complexes. In summary, as we move from the local universe to the high-redshift regime, our sources have higher Gini in the optical and less symmetry, due to their evolutionary phase. As we move from the optical to the UV, the sources have even higher Gini and asymmetry as we lose sight of extended

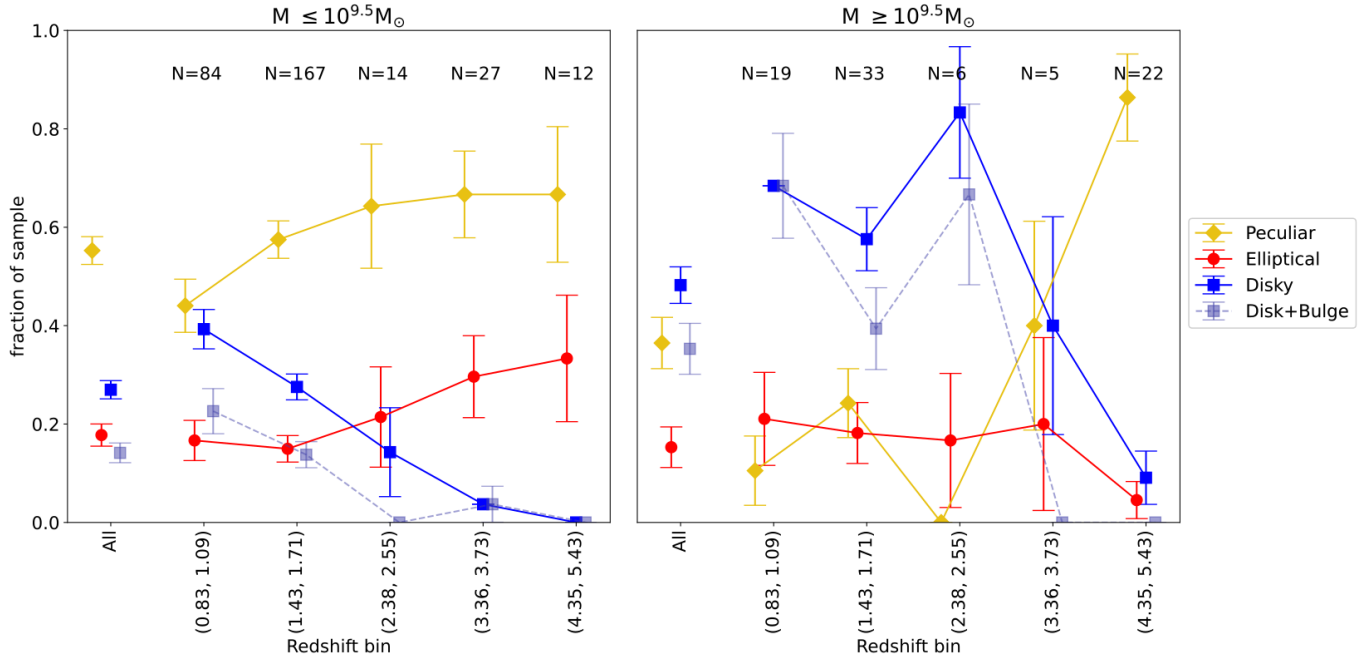


Figure 3. Morphology by mass and redshift bin, with the fraction of sources in each of our broad morphological categories shown. “Disky” refers to the union of “disk” and “disk+bulge” classifications. The contribution from disk+bulge galaxies to the disk fraction is shown with dashed lines. Here we divide the sample into two mass bins with approximately equal numbers. The number of our 388 sources in each of the redshift bins is also given. Error bars indicate the multinomial statistical $1-\sigma$ uncertainty, but they do not account for misclassification error.

structure and are biased toward seeing more actively star-forming regions.

Our results are in broad concordance with other recent JWST analyses. Both Nelson et al. (2022) and Fudamoto et al. (2022) find an unexpected population of very red disks at higher redshifts revealed in NIRCcam data (several examples are visible in Figure 1). Ferreira et al. (2022) similarly find a high proportion of disks which dominate at $z > 1.5$.

Finally, we note that our results show that using rest-frame optical GA values to automate morphology classification is very promising. The values show a much clearer mapping to visual morphologies compared to a similar analysis of the rest-frame UV.

4. SUMMARY AND CONCLUSION

The GLASS-JWST ERS parallel NIRCcam imaging has provided a fascinating snapshot of the high- z Universe. Among sources at $z > 2$ —a regime previously out of reach in the rest-frame optical—we make several new findings. In Paper XII, we examine morphology at the epoch of reionization ($z > 7$); here we have detailed a brief tour of this new part of parameter space with examination of RGB images in rest-frame *gri* colors of 388 sources at $0.8 < z < 5.4$ and present images of 99 representative examples binned by mass and redshift.

Although irregular and highly star-forming galaxies dominate as expected at these redshifts, we find many disks and sources with visible bulges as high as $z = 3.7$. The fact that many regular disks with spiral features, and a significant population of identifiable bulges were seen among the very first rest-frame optical images of the early Universe—while few might have been expected from high- z studies of rest-frame UV wavelengths with HST—provides new constraints for evolutionary models. Further imaging campaigns with JWST will provide larger samples to more thoroughly examine the census of bulges and bulge-to-disk ratios at high redshifts.

Our non-parametric analysis finds greater asymmetry than both the local population, but demonstrates that galaxies are smoother and more symmetrical than seen in previous high-redshift HST rest-frame UV images. We find a high correlation between location in the rest-frame optical $G-A$ plane and visual morphology, further supporting our visual classifications.

Overall we find that, even considering this modest ‘first look’ sample, regular galaxy morphological sequences are established at earlier times than expected. This brief snapshot of the infra-red Universe offers a glimpse at future exciting possibilities for galaxy evolution studies in the era of JWST astronomy.

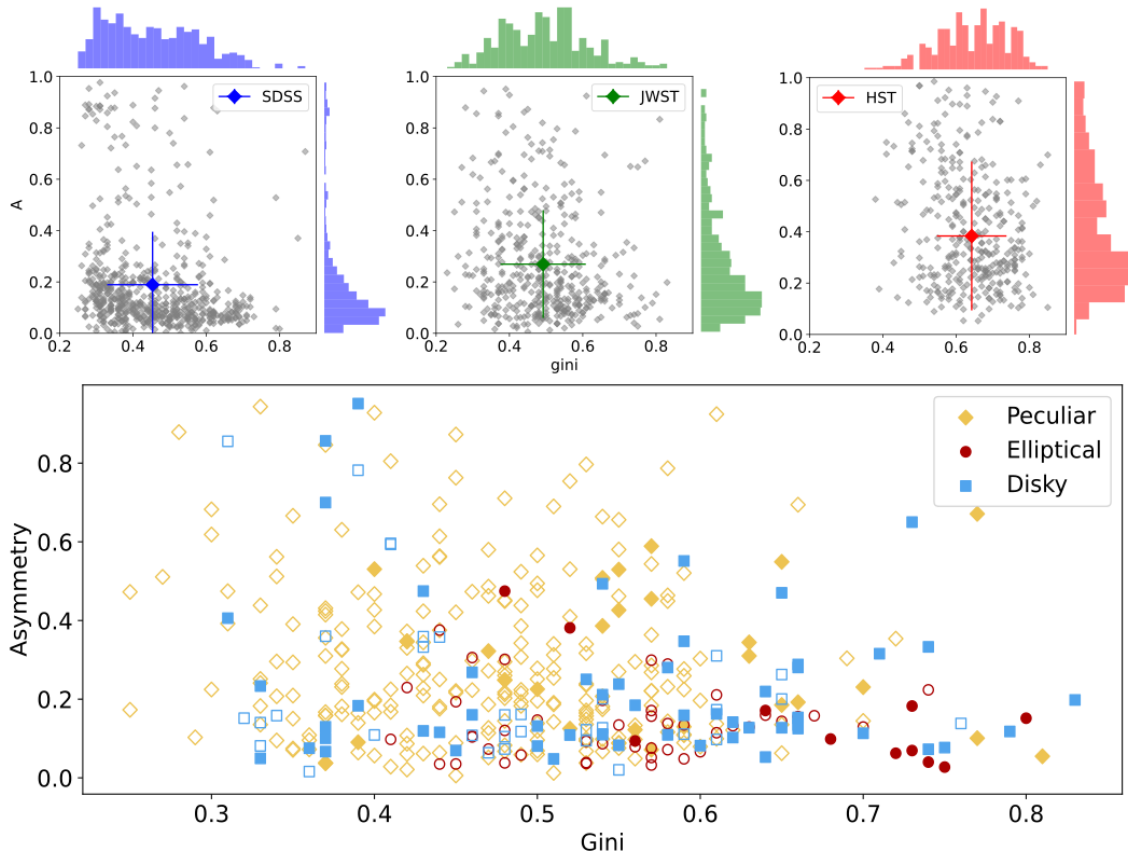


Figure 4. Morphological measurements of our sample, with Gini coefficient on the x -axis and asymmetry on the y -axis. **Top:** The gini-A plane for SDSS, our sample and the HST comparison sample respectively, with all sources plotted in gray and the mean A and gini values indicated in color. Histograms for each sample are also shown. The rest-frame UV imaging has higher G and A, due to clumpier morphology than rest-frame optical. **Bottom:** Our sample color-coded by morphological classification, with ellipticals in red, disks in blue, and irregulars in green. The sources mass-matched with the HST sample are shown as filled shapes. Our morphological classifications are in broad agreement with the GA values.

This work is based on observations made with the NASA/ESA/CSA James Webb Space Telescope. The data were obtained from the Mikulski Archive for Space Telescopes at the Space Telescope Science Institute, which is operated by the Association of Universities for Research in Astronomy, Inc., under NASA contract NAS 5-03127 for JWST. These observations are associated with program JWST-ERS-1324. We acknowledge financial support from NASA through grant JWST-ERS-1324. CJ, KG and TN acknowledge support from Australian Research Council Laureate Fel-

lowship FL180100060. MT acknowledges support from the Australian Research Council Centre of Excellence for All Sky Astrophysics in 3 Dimensions (ASTRO 3D), through project number CE170100013. ARHS acknowledges funding through the Jim Buckee Fellowship at ICRAR/UWA. MB acknowledges support from the Slovenian national research agency ARRS through grant N1-0238.

Software: LuptonHumVI code (Marshall et al. 2015), EAZY (Brammer et al. 2008), PhotUtils (Bradley et al. 2020), FAST++ code (Schreiber et al. 2018)

REFERENCES

Abraham, R. G., Tanvir, N. R., Santiago, B. X., et al. 1996a, Monthly Notices of the Royal Astronomical Society, 279, L47.
<https://doi.org/10.1093/mnras/279.3.L47>

Abraham, R. G., Valdes, F., Yee, H. K. C., & van den Bergh, S. 1994, The Astrophysical Journal, 432, 75.

<https://ui.adsabs.harvard.edu/abs/1994ApJ...432...75A>

- Abraham, R. G., van den Bergh, S., Glazebrook, K., et al. 1996b, *The Astrophysical Journal Supplement Series*, 107, 1.
<https://ui.adsabs.harvard.edu/abs/1996ApJS..107....1A>
- Abraham, R. G., van den Bergh, S., & Nair, P. 2003, *ApJ*, 588, 218.
<http://iopscience.iop.org/article/10.1086/373919/meta>
- Abraham, R. G., Nair, P., McCarthy, P. J., et al. 2007, *ApJ*, 669, 184.
<http://iopscience.iop.org/article/10.1086/521138/meta>
- Barden, M., Jahnke, K., & Häußler, B. 2008, *ApJS*, 175, 105.
<http://iopscience.iop.org/article/10.1086/524039/meta>
- Bertin, E., & Arnouts, S. 1996, *A&AS*, 117, 393
- Bianchi, L., & GALEX Team. 1999, *Memorie della Societa Astronomica Italiana*, 70, 365. <https://ui.adsabs.harvard.edu/abs/1999MmSAI..70..365B>
- Blanton, M. R., & Moustakas, J. 2009, *Annual Review of Astronomy and Astrophysics*, 47, 159.
<https://doi.org/10.1146/annurev-astro-082708-101734>
- Blanton, M. R., Bershady, M. A., Abolfathi, B., et al. 2017, *AJ*, 154, 28. <http://iopscience.iop.org/article/10.3847/1538-3881/aa7567/meta>
- Bradley, L., Sipőcz, B., Robitaille, T., et al. 2020, *Astropy/Photutils: 1.0.0*, Zenodo, , ,
 doi:10.5281/zenodo.4044744.
<https://doi.org/10.5281/zenodo.4044744>
- Brammer, G. B., van Dokkum, P. G., & Coppi, P. 2008, *ApJ*, 686, 1503.
<https://iopscience.iop.org/article/10.1086/591786/meta>
- Bruzual, G., & Charlot, S. 2003, *Monthly Notices of the Royal Astronomical Society*, 344, 1000.
<https://doi.org/10.1046/j.1365-8711.2003.06897.x>
- Buitrago, F., Trujillo, I., Conselice, C. J., & Häußler, B. 2013, *Monthly Notices of the Royal Astronomical Society*, 428, 1460. <https://doi.org/10.1093/mnras/sts124>
- Calvi, R., Poggianti, B. M., Fasano, G., & Vulcani, B. 2012, *Monthly Notices of the Royal Astronomical Society: Letters*, 419, L14.
<https://doi.org/10.1111/j.1745-3933.2011.01168.x>
- Calzetti, D., Armus, L., Bohlin, R. C., et al. 2000, *ApJ*, 533, 682.
<http://iopscience.iop.org/article/10.1086/308692/meta>
- Chabrier, G. 2003, *Publications of the Astronomical Society of the Pacific*, 115, 763.
<http://www.jstor.org/stable/10.1086/376392>
- Coe, D., Umetsu, K., Zitrin, A., et al. 2012, *ApJ*, 757, 22.
<https://doi.org/10.1088/0004-637x/757/1/22>
- Conroy, C. 2013, *ARA&A*, 51, 393
- Conselice, C. J. 2003, *ApJS*, 147, 1.
<http://iopscience.iop.org/article/10.1086/375001/meta>
- . 2008, 390, 403.
<https://ui.adsabs.harvard.edu/abs/2008ASPC..390..403C>
- . 2014, *Annual Review of Astronomy and Astrophysics*, 52, 291.
<https://doi.org/10.1146/annurev-astro-081913-040037>
- Conselice, C. J., Bershady, M. A., & Jangren, A. 2000, *ApJ*, 529, 886.
<http://iopscience.iop.org/article/10.1086/308300/meta>
- Conselice, C. J., Blackburne, J. A., & Papovich, C. 2005, *ApJ*, 620, 564.
<http://iopscience.iop.org/article/10.1086/426102/meta>
- Conselice, C. J., Bluck, A. F. L., Ravindranath, S., et al. 2011, *Monthly Notices of the Royal Astronomical Society*, 417, 2770.
<https://doi.org/10.1111/j.1365-2966.2011.19442.x>
- Correa, C. A., & Schaye, J. 2020, *Monthly Notices of the Royal Astronomical Society*, 499, 3578.
<https://doi.org/10.1093/mnras/staa3053>
- Dieleman, S., Willett, K. W., & Dambre, J. 2015, *Monthly Notices of the Royal Astronomical Society*, 450, 1441.
<http://adsabs.harvard.edu/abs/2015MNRAS.450.1441D>
- Dimauro, P., Daddi, E., Shankar, F., et al. 2022, *Monthly Notices of the Royal Astronomical Society*, 513, 256.
<https://doi.org/10.1093/mnras/stac884>
- Doyon, R., Hutchings, J. B., Beaulieu, M., et al. 2012, in *Space Telescopes and Instrumentation 2012: Optical, Infrared, and Millimeter Wave*, Vol. 8442 (SPIE), 1005–1017. <https://www.spiedigitallibrary.org/conference-proceedings-of-spie/8442/84422R/The-JWST-Fine-Guidance-Sensor-FGS-and-Near-Infrared-Imager/10.1117/12.926578.full>
- Dressler, A. 1984, IN: *Annual review of astronomy and astrophysics*. Volume 22. Palo Alto, CA, Annual Reviews, Inc., 1984, p. 185-222., 22, 185. <https://ui.adsabs.harvard.edu/abs/1984ARA%26A..22..185D/abstract>
- Driver, S. P., Bellstedt, S., Robotham, A. S. G., et al. 2022, *Monthly Notices of the Royal Astronomical Society*, 513, 439. <https://doi.org/10.1093/mnras/stac472>
- Elmegreen, D. M., & Elmegreen, B. G. 2013, *ApJ*, 781, 11.
<https://doi.org/10.1088/0004-637x/781/1/11>
- Elmegreen, D. M., Elmegreen, B. G., Ravindranath, S., & Coe, D. A. 2007, *ApJ*, 658, 763.
<https://iopscience.iop.org/article/10.1086/511667/meta>
- Fall, S. M. 1983, 100, 391.
<https://ui.adsabs.harvard.edu/abs/1983IAUS..100..391F>
- Ferreira, L., Adams, N., Conselice, C. J., et al. 2022, *ApJL*, 938, L2. <https://dx.doi.org/10.3847/2041-8213/ac947c>

- Freeman, P. E., Izbicki, R., Lee, A. B., et al. 2013, *Monthly Notices of the Royal Astronomical Society*, 434, 282. <https://doi.org/10.1093/mnras/stt1016>
- Fudamoto, Y., Inoue, A. K., & Sugahara, Y. 2022, *ApJL*, 938, L24. <https://dx.doi.org/10.3847/2041-8213/ac982b>
- Gardner, J. P. 2006, *IAU Special Session*, 1, 16. <https://ui.adsabs.harvard.edu/abs/2006IAUSS...1E..16G>
- Glazebrook, K. 2013, *PASA*, 30, e056
- Hubble, E. P. 1926, *The Astrophysical Journal*, 64, 321. <https://ui.adsabs.harvard.edu/abs/1926ApJ....64..321H>
- Huertas-Company, M., Pérez-González, P. G., Mei, S., et al. 2015, *ApJ*, 809, 95. <https://dx.doi.org/10.1088/0004-637X/809/1/95>
- Jakobsen, P., Ferruit, P., de Oliveira, C. A., et al. 2022, *A&A*, 661, A80. <https://www.aanda.org/articles/aa/abs/2022/05/aa42663-21/aa42663-21.html>
- Kartaltepe, J. S., Mozena, M., Kocevski, D., et al. 2015, *ApJS*, 221, 11. <https://dx.doi.org/10.1088/0067-0049/221/1/11>
- Law, D. R., Steidel, C. C., Erb, D. K., et al. 2007, *ApJ*, 656, 1. <https://iopscience.iop.org/article/10.1086/510357/meta>
- Lee, B., Giavalisco, M., Williams, C. C., et al. 2013, *ApJ*, 774, 47. <https://dx.doi.org/10.1088/0004-637X/774/1/47>
- Lintott, C., Schawinski, K., Bamford, S., et al. 2011, *Monthly Notices of the Royal Astronomical Society*, 410, 166. <https://doi.org/10.1111/j.1365-2966.2010.17432.x>
- Lotz, J. M., Primack, J., & Madau, P. 2004, *AJ*, 128, 163. <http://iopscience.iop.org/article/10.1086/421849/meta>
- Lupton, R., Blanton, M. R., Fekete, G., et al. 2004, *PASP*, 116, 133. <http://iopscience.iop.org/article/10.1086/382245/meta>
- Mager, V. A., Conselice, C. J., Seibert, M., et al. 2018, *ApJ*, 864, 123. <https://dx.doi.org/10.3847/1538-4357/aad59e>
- Marshall, P., Sandford, C., More, A., More, B., & More, H. 2015, *Astrophysics Source Code Library*, ascl:1511.014. <http://adsabs.harvard.edu/abs/2015ascl.soft11014M>
- Medezinski, E., Umetsu, K., Okabe, N., et al. 2016, *ApJ*, 817, 24
- Merlin, E., Bonchi, A., Paris, D., et al. 2022, arXiv e-prints, arXiv:2207.11701
- Mortlock, A., Conselice, C. J., Hartley, W. G., et al. 2013, *Monthly Notices of the Royal Astronomical Society*, 433, 1185. <https://doi.org/10.1093/mnras/stt793>
- Murata, K. L., Kajisawa, M., Taniguchi, Y., et al. 2014, *ApJ*, 786, 15. <https://doi.org/10.1088/0004-637x/786/1/15>
- Nanayakkara, T., Glazebrook, K., Jacobs, C., et al. 2022, Early Results from GLASS-JWST XVI: Discovering a Bluer $Z \sim 4-7$ Universe through UV Slopes, arXiv, arXiv:2207.13860. <http://arxiv.org/abs/2207.13860>
- Nelson, E. J., Suess, K. A., Bezanson, R., et al. 2022, JWST Reveals a Population of Ultra-Red, Flattened Disk Galaxies at $z \sim 2$, . <https://arxiv.org/abs/2208.01630v1>
- Oesch, P. A., Carollo, C. M., Feldmann, R., et al. 2010, *ApJL*, 714, L47
- Oke, J. B., & Gunn, J. E. 1983, *The Astrophysical Journal*, 266, 713. <https://ui.adsabs.harvard.edu/abs/1983ApJ...266..713O>
- Paris, D., Merlin, E., Fontana, A., et al. 2023, The GLASS-JWST Early Release Science Program. II. Stage I Release of NIRCam Imaging and Catalogs in the Abell 2744 Region, arXiv, arXiv:2301.02179. <http://arxiv.org/abs/2301.02179>
- Peng, C. Y., Ho, L. C., Impey, C. D., & Rix, H.-W. 2010, *AJ*, 139, 2097. <https://doi.org/10.1088/0004-6256/139/6/2097>
- Pillepich, A., Nelson, D., Springel, V., et al. 2019, *Monthly Notices of the Royal Astronomical Society*, 490, 3196. <https://doi.org/10.1093/mnras/stz2338>
- Roberts-Borsani, G., Morishita, T., Treu, T., et al. 2022, arXiv e-prints, arXiv:2207.11387
- Schreiber, C., Labbé, I., Glazebrook, K., et al. 2018, *A&A*, 611, A22. <https://www.aanda.org/articles/aa/abs/2018/03/aa31917-17/aa31917-17.html>
- Simons, R. C., Kassin, S. A., Weiner, B. J., et al. 2017, *ApJ*, 843, 46
- Straatman, C. M. S., Spitler, L. R., Quadri, R. F., et al. 2016, *ApJ*, 830, 51. <https://doi.org/10.3847/0004-637x/830/1/51>
- Sweet, S. M., Glazebrook, K., Obreschkow, D., et al. 2020, *Monthly Notices of the Royal Astronomical Society*, 494, 5421. <https://doi.org/10.1093/mnras/staa1050>
- Tacchella, S., Lang, P., Carollo, C. M., et al. 2015, *ApJ*, 802, 101. <https://doi.org/10.1088/0004-637x/802/2/101>
- Treu, T., Roberts-Borsani, G., Bradac, M., et al. 2022, *ApJ*, in press, arXiv:2206.07978
- Treu, T., Calabro, A., Castellano, M., et al. 2022, Early Results From GLASS-JWST. XII: The Morphology of Galaxies at the Epoch of Reionization, arXiv, arXiv:2207.13527. <http://arxiv.org/abs/2207.13527>
- van Dokkum, P. G., Leja, J., Nelson, E. J., et al. 2013, *ApJL*, 771, L35. <https://doi.org/10.1088/2041-8205/771/2/135>
- Whitney, A., Ferreira, L., Conselice, C. J., & Duncan, K. 2021, *ApJ*, 919, 139. <https://dx.doi.org/10.3847/1538-4357/ac1422>

Willott, C. J., Doyon, R., Albert, L., et al. 2022, *PASP*,
134, 025002. <https://doi.org/10.1088/1538-3873/ac5158>

Wisnioski, E., Förster Schreiber, N. M., Wuyts, S., et al.
2015, *ApJ*, 799, 209

Xue, Y. Q., Luo, B., Brandt, W. N., et al. 2011, *ApJS*, 195,
10

York, D. G., Adelman, J., John E. Anderson, J., et al.
2000, *AJ*, 120, 1579. <https://doi.org/10.1086%2F301513>

Zana, T., Lupi, A., Bonetti, M., et al. 2022, *Monthly
Notices of the Royal Astronomical Society*, 515, 1524.
<https://doi.org/10.1093/mnras/stac1708>

Zhu, X.-P., Dai, J.-M., Bian, C.-J., et al. 2019, *Astrophys
Space Sci*, 364, 55.
<https://doi.org/10.1007/s10509-019-3540-1>